Photoacoustics 38 (2024) 100619

Contents lists available at ScienceDirect

Photoacoustics

journal homepage: www.elsevier.com/locate/pacs

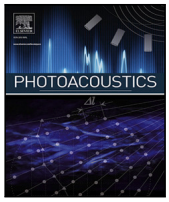

Research article

New silicon-based micro-electro-mechanical systems for photo-acoustic trace-gas detection

Jacopo Pelini [a,b,1], Stefano Dello Russo [b,c,1], Inaki Lopez Garcia [b], Maria Concetta Canino [d], Alberto Roncaglia [d], Pablo Cancio Pastor [b], Iacopo Galli [b], Wei Ren [e], Paolo De Natale [b], Zhen Wang [e,*], Simone Borri [b], Mario Siciliani de Cumis [c,*]

[a] University "Federico II", Corso Umberto I 40, Naples, 80138, Italy
[b] CNR-INO - Istituto Nazionale di Ottica, and LENS, via N. Carrara 1, Sesto Fiorentino, 50019, Italy
[c] ASI Agenzia Spaziale Italiana - Centro di Geodesia Spaziale, Località Terlecchia, Matera, 75100, Italy
[d] Istituto per la Microelettronica e Microsistemi (IMM) Consiglio Nazionale delle Ricerche (CNR), Via P. Gobetti 101, Bologna, 40129, Italy
[e] Department of Mechanical and Automation Engineering, The Chinese University of Hong Kong, New Territories, Hong Kong Special Administrative Region of China

ARTICLE INFO

Keywords:
Micro-electro-mechanical systems (MEMS)
Photo-acoustic spectroscopy
Trace-gas sensing
Quality factor
Resonant frequency
Acoustic-to-voltage transducer
Minimum detection limit
Parts-per-billion sensitivity

ABSTRACT

The achievable sensitivity level of photo-acoustic trace-gas sensors essentially depends on the performances of the acoustic transducer. In this work, the mechanical response of different silicon-based micro-electro-mechanical systems (MEMS) is characterized, aiming at investigating both their mechanical properties, namely the resonance frequency and the quality factor, and the minimum detection limit (MDL) achievable when they are exploited as an acoustic-to-voltage transducer in a trace-gas photoacoustic setup. For this purpose, a 4.56 μm Continuous-Wave (CW) quantum cascade laser (QCL) is used to excite a strong N_2O roto-vibrational transition with a line strength of 2.14×10^{-19} cm/molecule, and the detection of MEMS oscillations is performed via an interferometric readout. As a general trend, the minimum detection limit decreases when the resonance frequency investigated increases, achieving a value of 15 parts per billion with a 3 dB cut-off lock-in bandwidth equal to 100 mHz, around 10 kHz.

1. Introduction

Gas sensing technology has developed enormously in recent years [1]: the industrial growth and technological progress have pushed the development of highly performing and reliable sensors for environmental monitoring [2], industrial process control [3], medical diagnostics [4], detection of toxic and flammable gases [5], as well as explosives [6]. Among the various detection techniques, optical sensors stand out for their reduced response time (typically between 0.1 s and 10 s), high sensitivity, specificity, and accuracy. Optical sensing techniques are based on the absorption of photons of a specific wavelength by the target gas. Molecules in the gaseous state show, typically in the mid-IR spectral region, absorption peaks due to roto-vibrational excitation of the molecule itself. These peaks are often unique signatures identifying not only the molecule but also the isotopomer.

When molecules absorb light at a specific wavelength, they relax to the ground state by re-emitting the absorbed energy through radiative or non-radiative processes. In a typical photoacoustic setup, where the gaseous sample is kept at pressures and temperatures close to ambient ones, the prominent relaxation process is non-radiative, i.e. the excited molecules relax by transferring energy to the surrounding molecules through collisions [7,8]. This phenomenon creates a local increase in temperature and consequently a pressure gradient, generating a soliton. If the optical radiation is properly modulated, an acoustic wave is generated, and it can be selectively detected by a microphone. The main advantages of this technique, known as trace-gas photoacoustic spectroscopy (PAS) [9], compared to direct absorption techniques are: a zero-background in the absence of target gas, and an efficient gas analysis in extremely small volumes. Moreover, in PAS, no photodetectors are required, thus enhancing the simplicity, robustness, and adaptability of the system. Generally speaking, the PAS technique has gained an important role in applications, compared to direct absorption spectroscopy techniques (DAS), when relatively high high-power light sources and small path-lengths are available [10].

* Corresponding authors.
E-mail addresses: zhenwang@cuhk.edu.hk (Z. Wang), mario.sicilianidecumis@asi.it (M. Siciliani de Cumis).
[1] Jacopo Pelini and Stefano Dello Russo contributed equally to this work.

https://doi.org/10.1016/j.pacs.2024.100619
Received 25 March 2024; Received in revised form 30 April 2024; Accepted 10 May 2024
Available online 21 May 2024

In the first years of trace-gas PAS development, researchers focused on optimizing the photoacoustic cell, to make it resonant with the acoustic wave generated, and detected by traditional condenser microphones [11]. In the early 2000s, however, the scientific effort focused on the maximization of detection performance by acting directly on the sensitive element. Kosterev et al. [12] reported for the first time the study of a PA sensor using a quartz tuning fork (QTF) as an acoustic transducer, which is a sharp piezoelectric resonator, thus enabling a new photoacoustic-based technique known as Quartz-enhanced Photoacoustic Spectroscopy (QEPAS). In the same years, Wilcken and Kauppinen [13] proposed a different photoacoustic sensing approach, known as Cantilever-Enhanced Photoacoustic Spectroscopy (CEPAS), based on a cantilever as the sensitive element with an interferometric readout. Both these innovative approaches have been thoroughly studied in recent years [10,14,15], reaching detection performances comparable with conventional PAS, but with the advantage of an easier miniaturization [16]. The main difference between QEPAS and CEPAS lies in the acousto-mechanical properties of the sensitive element, quantifiable via its resonance frequency (f) and quality factor (Q), and on their different readout principle, which for QEPAS is electronic for CEPAS is (mostly) optical. Indeed, whereas the QEPAS technique uses QTFs with resonance frequencies of the order of tens of kHz and quality factors typically higher than 10000 [17–19], the CEPAS technique uses cantilevers with resonance frequencies in the kHz range and quality factors of around 1000 [20–22]. Higher resonance frequencies are advantageous, due to a drastic reduction in the noise level, although the PA signal appears to be more dependent on the relaxation dynamics of the gases, which could not allow a complete release of the absorbed energy during each oscillation period. This behavior makes the PA signal dependent on the concentration of other gas species in the mixture, determining the overall accuracy of the sensor [23,24]. Pioneering computational approaches have demonstrated efficient compensation of such effects for several gas species [25,26] although the literature is often lacking specific data on molecular relaxation dynamics. Generally speaking, the trade-off between noise reduction and minimization of non-linearities leads to an optimal resonance frequency in the kHz — tens of kHz range.

In this scenario, this paper reports an analysis of acousto-mechanical properties for five new Si-based custom Micro-Electro-Mechanical Systems (MEMS). After the geometric optimization in terms of mechanical properties, through simulation with finite element methods (FEM), the realized MEMS structures were finally inserted in a photoacoustic setup. Six different MEMS vibrational modes were chosen for the analysis, with estimated frequencies ranging from approximately 1 to 10 kHz. Via the photoacoustic excitation, the resonance properties of the chosen modes were evaluated and compared with the simulated ones. Subsequently, the photoacoustic detection performances of the MEMS, in terms of Minimum Detection Limit (MDL) and normalized noise equivalent absorption (NNEA), were estimated and compared with the state-of-the-art main PA-based sensing techniques. Nitrous oxide (N_2O), a gas of interest for air pollution and global warming, with a Global Warming Potential (GWP) 273 times that of CO_2 for a 100-year timescale, was chosen as the target gas.

2. Designing the MEMS structures

Silicon is a material with mechanical properties that make it ideal for building MEMS structures [27]. In particular, by carefully choosing the material (crystalline orientation, doping) and tailoring the geometry, it is possible to design different structures with different mechanical behavior. These devices will act as suspended mirrors placed in a gas chamber, acting as the acoustic-to-voltage transducer for the sound wave generated by the photo-acoustic effect. In the meantime, the device operates as the end mirror of a Michelson interferometer for the photo-acoustic signal readout, as described in detail in Section 3. Material properties, mass, and suspension structures will determine the mechanical behavior of the Silicon element, as the frequency spectrum of the mechanical resonance and the oscillator Quality factor (Q). To get a rough evaluation of the mechanical spectra, Finite Element Modeling was performed for every structure in static conditions, collecting the eigenfrequency values for each device under study. The iterative

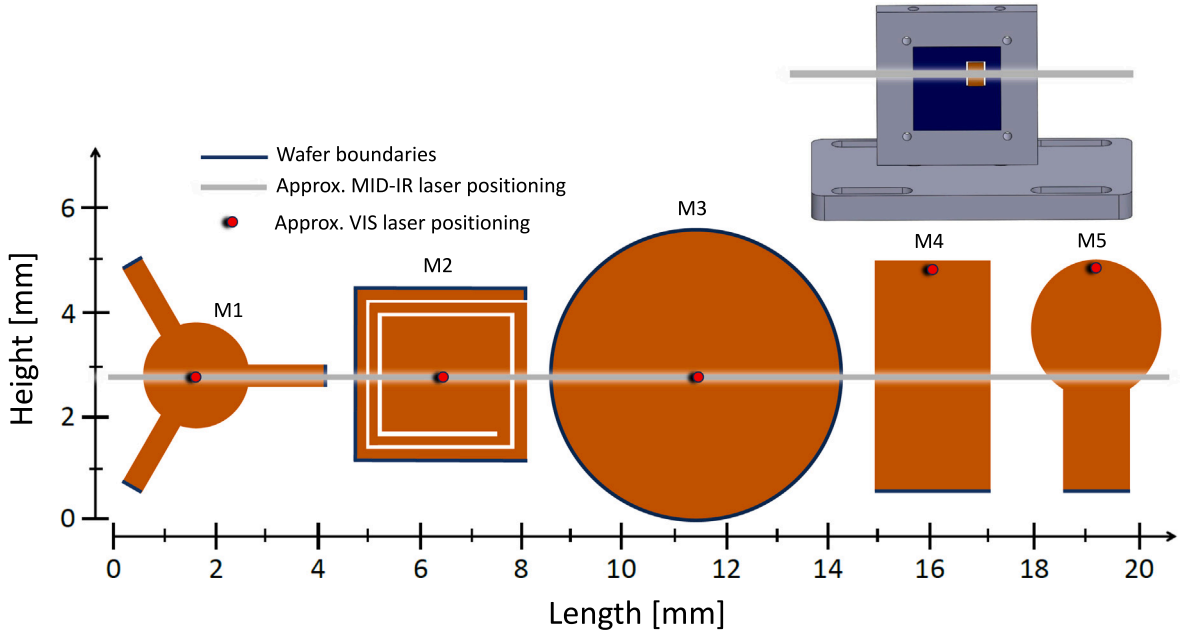

Fig. 1. Schematic bi-dimensional representation of the five investigated MEMS structures, depicted in orange. The vertical and horizontal scales (length and height, respectively) allow the reader to have an idea of their dimensions. All of them are characterized by a thickness of 10 μm. Segments highlighted in blue represent the parts where they are anchored to the substrate. The gray blurred line represents the approximated location of the mid-infrared laser beam used for the pressure wave generation. The red spot indicates the position where the He-Ne laser, used for the interferometric readout, hits the structures. **Inset**: a three-dimensional sketch of the custom-made aluminum anchoring system. The ensemble is placed within the sample such that the QCL beam passes as close as possible to the MEMS without ever touching it.

process involving the above-mentioned parameters enables tailoring the resonances in the desired zone. In particular, for each designed structure the geometric parameters were varied to obtain fundamental resonance frequencies in the 1–10 kHz range. The simulation results are shown in Table 1 of Section 4.1, together with the experimental results.

The geometrical features of the five different structures studied in this work are sketched in Fig. 1. The regions in which the structures are anchored to the substrate are colored dark blue. To place safely each of them inside the aluminum gas chamber, where the photo-acoustic effect occurs, they are mounted on a custom-made anchoring system whose 3D-rendering is shown in the **Inset** of Fig. 1. Its architecture was properly chosen to keep the MEMS coaxial to the mid-infrared beam, sketched in the figure in blurred gray, and as close as possible to the point-size sound wave source. Finally, the red point indicates, for each structure, the location of the He–Ne laser used for the interferometric readout, and aligned to hit the region stressed by the highest possible oscillation amplitude at the specific resonant mode. The structure's geometries were chosen to enhance different acousto-mechanical features. For example, the spring-like structure of M2 was selected to maximize the oscillation amplitude, while for the "drum" membrane M3, which is completely anchored to the support, a reduced vibration amplitude is expected as well as a lower noise level. In M1, the interplay between the anchored and unanchored parts is expected to guarantee a compromise between a considerable oscillation amplitude and the noise. M4 is designed according to the rectangular structure for standard CEPAS systems [28,29], for comparison purposes with the other novel structures. Finally, in M5 the thinner base and larger head are designed to increase the interaction between the sensitive element and the impacting acoustic wave, thus enhancing the cantilever response compared to the standard rectangular shape.

Finally, the fabrication processes, described in detail in Appendix A and depicted in Fig. A.7, were realized in the clean room of the Institute of Microelectronics and Micro-systems of the Italian National Research Council (CNR-IMM) in Bologna.

3. Experimental setup

As stated previously, the scope of this experiment is both to characterize the mechanical properties of the silicon-based MEMS with different geometries and to test their performances as acoustic-to-voltage transducers in a trace-gas photo-acoustic sensor. In Fig. 2 a schematic representation of the experimental setup is depicted. A Continuous-Wave, Single-Mode, Quantum Cascade Laser (QCL) emitting around $4.56\,\mu m$ is chosen to generate pressure waves via the photo-acoustic effect, addressing a N_2O strong roto-vibrational transition at $2189.273\,cm^{-1}$ with a line strength of 2.14×10^{-19} cm/molecule, well isolated from any absorption lines of other molecules (e.g. water vapor) at the working pressure range. An integrated modular controller (provided by ppq Sense S.R.L, QubeCL 52) is exploited both to drive the laser's bias current and to stabilize the laser's temperature at 20 °C via a four-stage thermo-electric cooling. An optical isolator (ISO, COHERENT FM2 MID-IR $4.55\,\mu m$) is placed after the laser chip to avoid optical feedback, while an acousto-optical modulator (AOM, M1208-G80-4, deflection efficiency $\approx 94\%$) intensity-modulates the optical beam at the given MEMS structure's resonant frequency, thus allowing the acoustic wave generation following the trace-gas non-radiative relaxation.

Then, the optical beam enters the aluminum chamber, where the tested silicon-based MEMS are placed, through a Zinc Selenide (ZnSe) wedged window. The pressure inside the chamber is managed by a vacuum system, consisting of a vacuum pump (PFEIFFER DualGauge), a pressure controller (PFEIFFER HiCUBE), a gas cylinder containing 200 ppm of N_2O in pure N_2, and needle valves. In this way, it is possible to evaluate the acousto-optical response of the structures for a constant concentration of the target gas and pressures ranging from 5 mbar to 300 mbar. The localized perturbation leads the MEMS to oscillate with an amplitude proportional to the sound wave's intensity propagating in the gas mixture. These oscillations are converted into a voltage signal, i.e. the photo-acoustic signal, via a Michelson interferometric readout [30]. A Helium-Neon (HeNe) laser emitting at $633\,nm$ is used as the probe beam and it is divided into two identical paths via a 50/50 beam splitter (BS). One of the two beams, namely the reference beam, impinges a reflective gold mirror (RM), while the other portion of the beam, which represents the measurement optical path, is focused on the high-reflectivity coated surface of the MEMS via a lens (f = 100 mm) and a wedged NBK-7 window. Both the back reflected beams are re-collected at the same BS, and finally sent to a photo-detector. The detected interferometric signal is demodulated via a lock-in amplifier (MFLI, Zurich Instruments) at the MEMS resonance frequency, and the $R = \sqrt{x^2 + y^2}$ component signal is acquired, leading to a first harmonic (1f) acquisition scheme. The characterization of the mechanical responses of the MEMS was performed, for each value of working

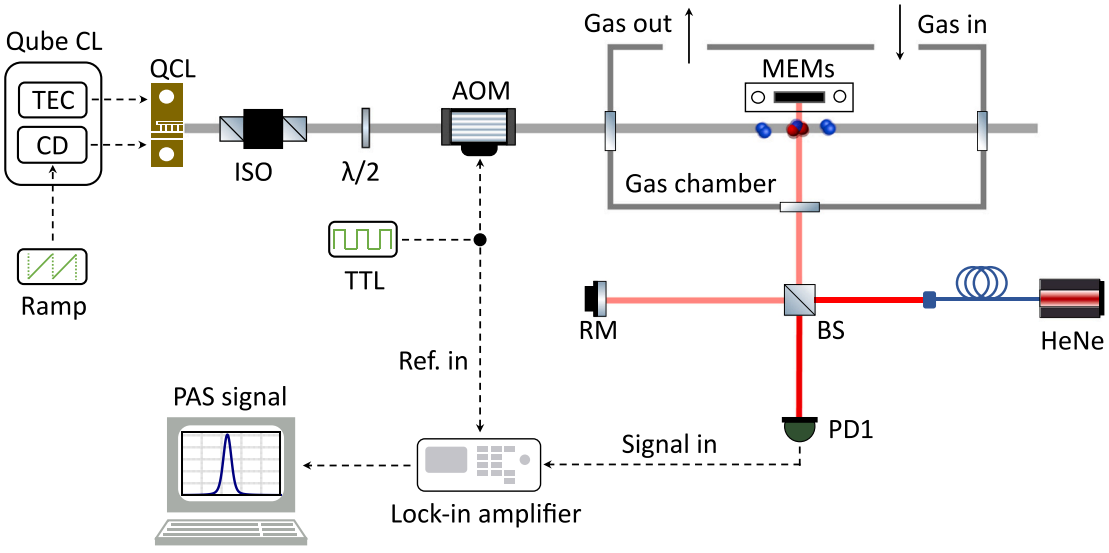

Fig. 2. Schematic representation of the photo-acoustic spectroscopy trace-gas setup implemented to characterize our MEMS structures. TEC: temperature Controller. CD: current driver. QCL: Quantum Cascade Laser. ISO: optical isolator. $\lambda/2$: half wave-plate. AOM: acousto-optic modulator. HeNe: Helium-Neon laser. BS: beam splitter. PD: photo-diode detector. RM: reflective mirror.

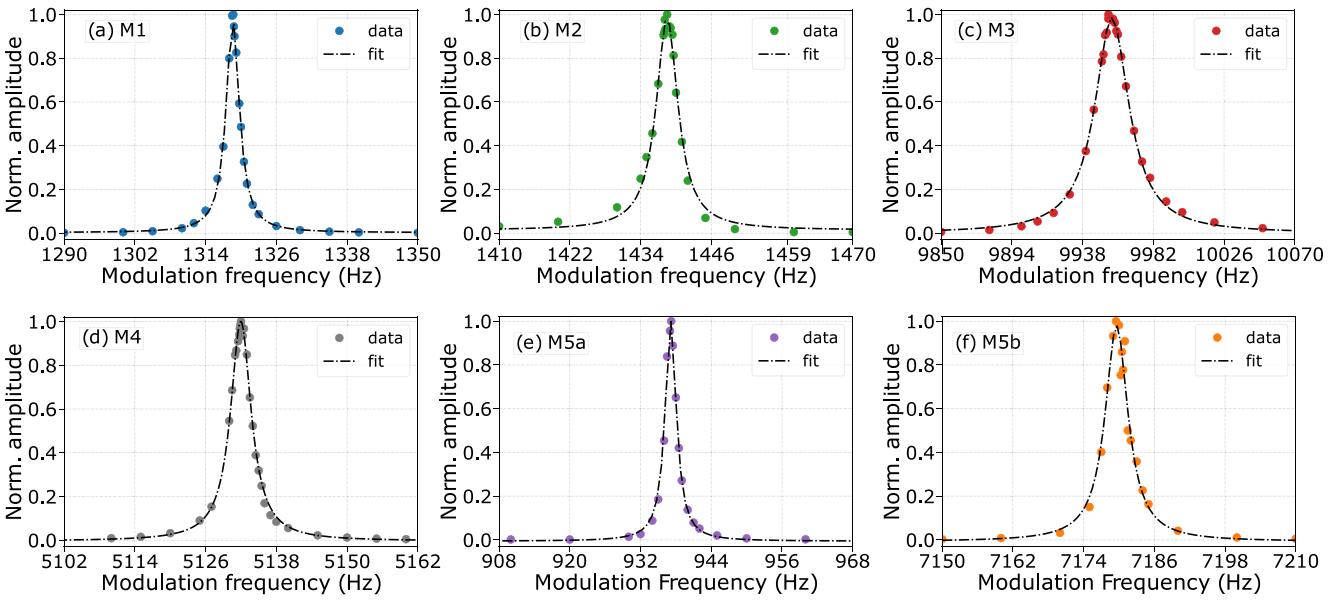

Fig. 3. Normalized R^2-component signals versus modulation frequency at a fixed working pressure of 20 mbar for **(a)** M1, **(b)** M2, **(c)** M3, **(d)** M4, **(e)** M5a, and **(f)** M5b. For each of them, the colored points represent the experimental data, while the dashed black line is the associated Lorentzian fit. Given the FWHM Δf and the central frequency f_0 as the fit results, then the Q-factor can be calculated as $Q = f_0/\Delta f$.

pressure, by locking the laser current on the N_2O absorption peak and varying the AOM on/off frequency. The photo-acoustic response study, instead, was done by fixing the AOM frequency at each MEMS resonant frequency and scanning the laser current. More details will be presented in Sections 4.1 and 4.2.

4. Results and discussion

4.1. Mechanical response

As it is known, the resonant properties of an oscillating structure, namely the resonance frequency, and the quality factor, can be extracted from the associated resonant curve's spectrum characterized by the following Lorentzian shape:

$$L(f) = L_0 + \frac{2A}{\pi}\frac{\Delta f}{4(f - f_0)^2 + \Delta f^2}, \quad (1)$$

where L_0 and A are two constants, while f_0 and Δf are the central (i.e. the resonant) frequency and the Full Width at Half Maximum (FWHM), respectively. The ratio between these two quantities allows the determination of the quality factor, $Q = f_0/\Delta f$, a dimensionless parameter that describes how under-damped an oscillator or resonator is. To experimentally reconstruct the resonant curves of the frequency, we performed a step-wise photo-acoustic measurement fixing the laser current at the absorption line peak (around 158.9 mA) and changing the AOM on/off frequency (i.e. the laser intensity-modulation frequency) within a range near the resonant frequency predicted by the simulation and associated with the chosen oscillation mode of each MEMS. These measurements were repeated for different working pressures within a range from 5 mbar to 300 mbar. Each data point, collected with a 3 dB cut-off lock-in bandwidth set to 100 mHz, represents the mean value of the de-modulated R-component signal, and the associated error was estimated by computing the 1σ standard deviation. The theoretical approach underlying the voltage readout of the resonator's acousto-mechanical response is identical to that expressed for current readout in Equation (6) of Ref. [31]. It is trivial to demonstrate that the in-phase component, X, and the square of the total signal component, R^2, differ by a constant multiplication factor, so the resonance features (f and Q) can be evaluated in the same way using one component or the other. Hence, to suppress any errors dictated by a change in phase of the system, the square of the overall signal R was directly evaluated.

Table 1
Investigated resonant modes and simulated displacements, theoretical (f_{th}) and estimated (f_0) resonant frequencies, Full Width at Half Maximum Δf, and quality factor Q of the five studied silicon-based structure at the fixed working pressure of 20 mbar. The theoretical resonant frequency was determined in vacuum conditions. For all the six modes the simulated displacement is shown. The qualitative color map, from blue (minimum displacement) to red (maximum displacement), allows the reader to have an idea about the entity of the membrane's deformation.

MEMS	Resonant mode	f_{th} (Hz)	f_0	Δ (Hz)	Q
M1	Fundamental	2051	1318.6	2.7	488
M2	Fourth overtone	1422	1438.5	4.6	313
M3	Fundamental	12429	9956.2	25.8	386
M4	Second overtone	4195	5132.0	4.3	1193
M5a	Fundamental	846	937.1	2.3	407
M5b	Second overtone	6846	7179.6	4.7	1528

The acoustic responses of the five different structures, at a fixed working pressure of 20 mbar, are reported in Fig. 3. The structure M5 was investigated both in its fundamental mode (M5a) and in its second overtone (M5b).

To make the comparison more effective, all the data were normalized to their respective peak values, while in Table 1 are reported the investigated resonant mode, the associated theoretical (f_{th}) and measured (f_0) frequencies, the Full Width at Half Maximum Δf, and the quality factor Q at a pressure of 20 mbar for each MEMS structure. The overall trend of both the Q-factor and the resonance frequency with the pressure is reported in Appendix A.

M1 shows a percentage difference of around 36% between the simulated and the experimental resonance frequencies, while in all the other cases this difference lies between more acceptable values from 1% (for M2) and 19% (for M3). This discrepancy is linked to a non-optimal release of M1 on its substrate during the fabrication process, leading to

a final structure slightly different from the simulated one. All the MEMS show a very narrow FWHM, from 2.3 Hz to 4.6 Hz, except for M3, whose measured mode width is 25.8 Hz. The different behavior arises from the fact that (as shown in Fig. 1), M1, M2, M4, and M5 share a structure where the boundaries are only partially anchored to the substrate, while M3 is entirely anchored to it. This crucial difference has an impact on the response of the investigated structure to the pressure wave generated following the trace-gas non-radiative relaxation. In the first case (M1, M2, M4, and M5), the limited anchoring points allow the MEMS to oscillate with negligible perturbation of the substrate. Conversely, in the second case (M3), the oscillation is the result of a strong interaction between the MEMS and the substrate, resulting in a broadening of the resonance curve spectrum.

At a pressure of 20 mbar, only M4 and M5b show Q-factor values above 1000 (1193 and 1528, respectively). Since the photo-acoustic signal is linearly proportional to the Q-factor, for these two modes a higher performance, in terms of signal-to-noise ratio (SNR) of the PAS signal, is expected. In all the other cases the Q-factor lies well below 1000: 488 for M1, 313 for M2, 386 for M3, and 407 for M5a. As the pressure increases, the quality factors decrease due to an increase in the damping effect caused by the interaction between the molecules present in the gas sample and the vibrating structure [32]. Both the Q-factor and the resonance frequency variations with the pressure for all the structures are reported and discussed in Appendix B.

4.2. Photo-acoustic response: PAS signals and MDLs

The performances of the five investigated MEMS when exploited as acoustic-to-voltage transducers can be evaluated by computing the minimum detection limit (MDL) achievable by each of them. The photoacoustic response was investigated by filling the PAS chamber with a sample of 200 ppm of N_2O in pure N_2, for several values of the sample pressures ranging from 5 mbar to 300 mbar. From each acquired photo-acoustic spectrum, the peak signal is extracted, and the photo-acoustic noise is computed by performing the 1-σ standard deviation of the signal far from the absorption peak. The ratio between the peak signal, from which the associated offset level is subtracted, and the noise defines the SNR at a specific pressure. Finally, the related MDL is obtained by dividing the trace-gas concentration (200 ppm in our case) for the SNR.

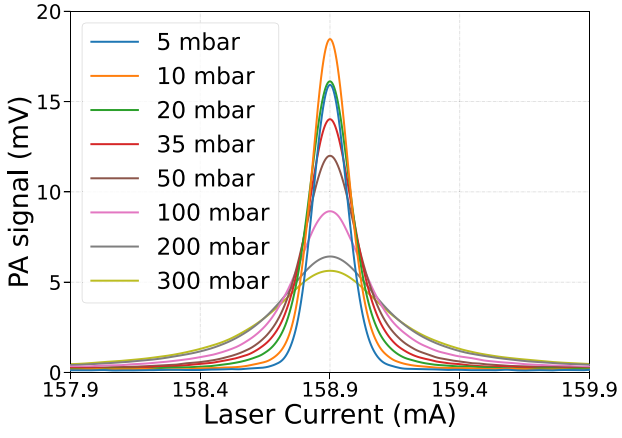

Fig. 4. PA signals versus laser current for M4 at different working pressure regimes. The spectra represent the R-component of the 1-f photo-acoustic signal acquired from the Michelson interferometer output and demodulated via the lock-in amplifier at the MEMS resonant frequency. The 3 dB cut-off lock-in bandwidth is set to 100 mHz. The current driver used to scan the laser current is characterized by a driver with a voltage-to-current conversion factor of 2 mA/V. The ramp for the acquisition of the N_2O absorption line is characterized by the following settings: frequency 2.5 mHz, amplitude 2 VPP (peak-to-peak voltage), phase 0 degrees, and symmetry 50%.

As a representative example, Fig. 4 shows the photo-acoustic spectra acquired with the structure M4 (rectangular cantilever) at different working pressure regimes. As it is possible to see, the photo-acoustic peak signal increases by moving from 5 to 10 mbar, where it reaches its maximum, then it starts to decrease when further increasing the pressure. This behavior, better highlighted in Fig. 5**(d)**, reflects, on one side, the less efficient sound wave generation at low-pressure regimes, and, on the other side, the damping effect on the MEMS oscillation for increasing gas pressures linked to the quality factor degradation [33]. It follows that, for structure M4, the optimal trade-off condition between these two trends occurs at 10 mbar. Similar evidence can be observed in all the investigated structures, as reported in Appendix C where all the photo-acoustic spectra are presented.

As reported in Fig. 5, the overall trend of the photo-acoustic peak signal in pressure (represented by the blue data points) behaves in a very similar way for all the investigated MEMS structures. More deeply, starting from 5 mbar, the PAS signal increases until it reaches a maximum value at relatively low pressures (within a range from 10 to 50 mbar), then it rapidly decreases at higher pressures.

Another figure of merit is represented by the photo-acoustic noise (red data points in Fig. 5), which strongly affects the estimation of the final detection sensitivity. As expected, the noise monotonically decreases when the pressure increases in all six investigated cases, mainly due to the smaller "free" vibration amplitude of the structures at higher pressures. The same behavior can be found for the Q-factors in Appendix B. Furthermore, an inverse proportionality between the noise level and the resonant frequency, justified by the combination of the electronic flicker noise (1/f noise) [34] and the acoustic noise (usually more pronounced at lower frequencies), can be observed as a general trend. In fact, starting from a level of the order of tens of μV for a resonant frequency around 900 Hz (M5b, Fig. 5**(e)**), the noise decreases by a factor of about 100 for a resonant frequency around 10 kHz (M3, Fig. 5**(c)**). Once the Signal-to-Noise ratio (SNR) is calculated from the data shown in Fig. 5, the minimum detection limit achievable by each MEMS structure can be calculated, as a function of the pressure. As a general trend, the MDL shows progressively lower values as the resonance frequency increases. In fact, the structures M1, M2, and M5a, characterized by resonant modes at lower frequencies, show a MDL laying in the 100–1000 ppb range (blue, green, and purple curves in Fig. 6**(a)**, respectively). On the other side, all the other three investigated cases (M3 in red, M4 in gray, and M5b in orange), characterized by higher resonant frequencies (10 kHz, 5 KHz, and 7 kHz respectively), show one order of magnitude better sensitivities, with a MDL going down to around 10 ppb for 10 s averaging time. This evidence highlights how the estimation of the detection sensitivity depends on a trade-off between the amplitude, the symmetry, and the environmental noise related to the structure's oscillations that affect both the amplitude of the photo-acoustic signal and the noise level.

As an example, it is possible to compare the performances of M5 when investigated in its fundamental resonant mode (M5a) and its second overtone (M5b), at a fixed pressure of 20 mbar. According to Figs. 5**(e)** and 5**(f)**, a factor ~4 between the PAS peak amplitude at 900 Hz and 7 kHz (122 mV and 27 mV respectively) is observed. This confirms that fundamental mode excitation leads to a bigger displacement when compared to its overtone, for the same-impinging pressure wave intensity. However, due to the larger environmental noise contribution at lower frequencies, the discrepancy between the photoacoustic peak amplitude is counterbalanced by the much lower noise level at 7 kHz (3.1 μV compared to a value of 53.2 μV obtained at 900 Hz), resulting in a higher signal-to-noise ratio, and consequently higher sensitivity.

Fig. 6**(b)** shows the MDL reached by each MEMS structure re-arranged in ascending order with the resonance frequency. The color map is the same as the one used in Fig. 6**(a)**. As it is possible to see, the lowest minimum detection limit achieved is 15 ppb obtained with the structure M3 investigated in its fundamental resonant mode at around 10 kHz.

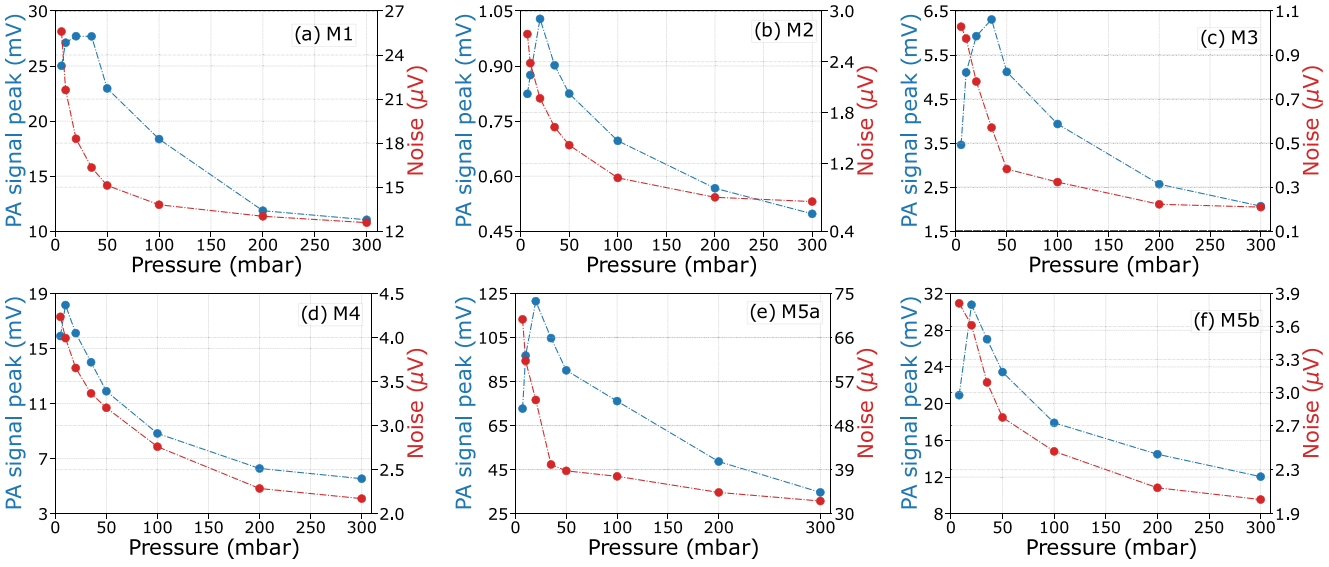

Fig. 5. Normalized photo-acoustic peak signal (red dots) and photo-acoustic noise (blue dots) as a function of the working pressure for **(a)** M1, **(b)** M2, **(c)** M3, **(d)** M4, **(e)** M5a, and **(f)** M5b. Each blue data point represents the peak of the photo-acoustic spectrum at a specific pressure, while the red data point is the computed 1-σ noise.

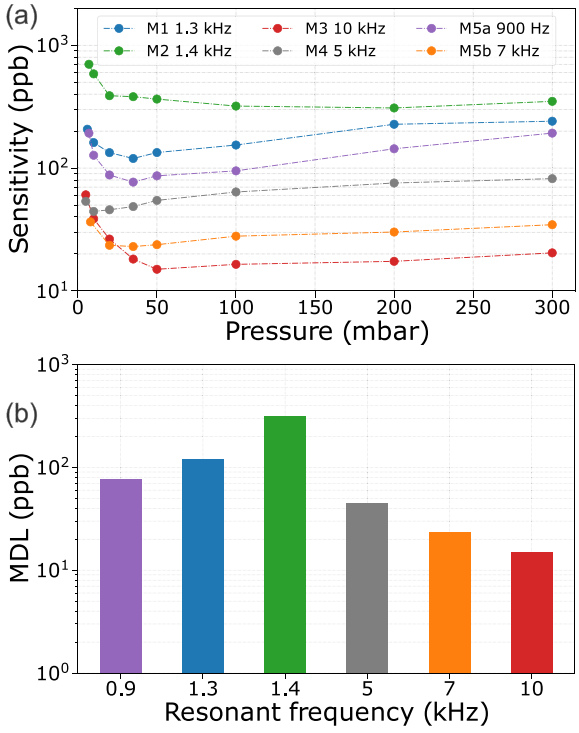

Fig. 6. (a): MDL as a function of the working pressure for the different structures investigated acquired over 10 s timescale. As reported in the legend: blue dots for M1, green dots for M2, red dots for M3, gray dots for M4, purple dots for M5a, and orange dots for M5b. **(b)**: minimum detection limit (MDL) reachable for each MEMS structure sorted in ascending order with the resonant frequency. The two graphs share the same color map.

5. Conclusions

In this work, the realization and the experimental characterization of both the mechanical and photo-acoustic responses of five silicon-based micro-electro-mechanical systems with different structures and geometry have been presented. Firstly, their resonant frequencies and quality factors have been characterized. Among all the six resonant modes investigated, the highest quality factors have been recorded by the second overtones of the two cantilevers (M4, and M5b) lying respectively above 800 and 1000 in the whole investigated pressure range. Secondly, all five investigated structures have been tested as acoustic-to-voltage transducers in a trace-gas photo-acoustic sensor investigating a fundamental N_2O roto-vibrational transition at 4.56 μm. This comparison highlighted that better performances are achieved when the MEMS are operated at higher resonant frequencies, characterized by higher Signal-to-Noise ratios. The best performances are achieved by the "racket-like" cantilever in its second overtone (M5b), and the membrane structure M3 at its fundamental mode at around 10 kHz, showing similar sensitivity levels. In fact, given a QCL impinging radiant power of 15 mW, a minimum detection limit of 15 ppb has been achieved with the MEMS structure M3 for a 3 dB cut-off lock-in bandwidth equal to 100 mHz (time constant 0.8 s, roll-off 18 dB/oct), corresponding to a normalized noise equivalent absorption (NNEA) coefficient of 1.7×10^{-8} $cm^{-1}W\,Hz^{1/2}$. This value is comparable to the state-of-the-art of the main cantilever- and QTF-based photoacoustic sensing techniques [35,36]. The achieved minimum detection limit lies well below the nominal concentration of N_2O in air (about 330 ppb [37]), allowing for environmental applications. For this purpose, the characterization performed in this work has highlighted the behavior of the different MEMS structures in a large pressure range, up to 300 mbar, allowing the selection of the optimal geometry according to the desired specific application. In particular, some structures show a very limited deterioration of their sensitivity when operated at high pressure. This is the case, for example, of the two best structures M3 and M5b, which maintain high performance up to the highest investigated pressure. This feature, together with their weak dependence on environmental noise, makes the structures M3 and M5b two good candidates for direct open-air sensing.

The results achieved with this work open the doors to the development of CEPAS setups with improved performance going beyond the state-of-the-art. The most promising investigated structures will be tested in an advantaged photoacoustic setup, where the use of acoustic resonators [11,38] and optical resonators [39,40] is expected to largely increase the sensitivity here achieved. To conclude, it is worth pointing out that the characterization measurements presented in this seminal

work demonstrate how beneficial is to continue exploring new components for the future development of compact and high-performing sensing systems.

Abbreviations

The following abbreviations are used in this manuscript:

PAS	Photo-acoustic spectroscopy
MEMS	Micro-electro mechanical system
ppb	Part-per-billion
MDL	Minimum detection limit
NNEA	Normalized noise equivalent absorption coefficient

Funding

This work was partially supported by EDA under the Cat-B Project Q-LAMPS "Quantum LAser-based Multi-parametric Portable Sensor" (EDA contract n.B-PRJ-RT-989), by EU NextGenerationEU Programme with the I-PHOQS Infrastructure "Integrated infrastructure initiative in Photonic and Quantum Sciences" [IR0000016, ID D2B8D520], the Laserlab-Europe Project [G.A. n.871124], the MUQUABIS Project [G.A. n.101070546] "Multiscale quantum bio-imaging and spectroscopy", by the European Union's EDF Projects ADEQUADE "Advanced, Disruptive and Emerging QUAntum technologies for DEfense" (ID 101103417) and CASSATA "Covert and Advanced multi-modal Sensor Systems for tArget acquisition and reconnAissance" (ID 101121447), by the "National Natural Science Foundation of China (NSFC) (8326015, 52122003)" and by the "Direct Grant for research from The Chinese University of Hong Kong".

CRediT authorship contribution statement

Jacopo Pelini: Writing – review & editing, Writing – original draft, Software, Methodology, Investigation, Data curation. **Stefano Dello Russo:** Writing – review & editing, Writing – original draft, Software, Methodology, Investigation, Data curation. **Inaki Lopez Garcia:** Resources, Methodology. **Maria Concetta Canino:** Resources, Data curation. **Alberto Roncaglia:** Resources, Methodology, Data curation. **Pablo Cancio Pastor:** Writing – review & editing, Validation, Supervision, Methodology, Conceptualization. **Iacopo Galli:** Resources, Methodology. **Wei Ren:** Validation, Supervision. **Paolo De Natale:** Supervision, Resources, Funding acquisition. **Zhen Wang:** Writing – review & editing, Supervision, Resources, Methodology, Investigation. **Simone Borri:** Writing – review & editing, Supervision, Resources, Methodology, Investigation, Funding acquisition, Conceptualization. **Mario Siciliani de Cumis:** Writing – review & editing, Validation, Supervision, Resources, Methodology, Investigation, Formal analysis, Conceptualization.

Declaration of competing interest

The authors declare the following financial interests/personal relationships which may be considered as potential competing interests: Paolo De Natale, Simone Borri reports financial support was provided by European Defence Fund. Paolo De Natale reports financial support was provided by European Defence Agency. Paolo De Natale reports financial support was provided by Horizon Europe. Wei Ren reports financial support was provided by National Natural Science Foundation of China (NSFC). Zhen Wang reports financial support was provided by Laserlab-Europe. Paolo De Natale reports financial support was provided by HORIZON EUROPE Framework Programme. Mario Siciliani de Cumis, Simone Borri, Inaki Lopez Garcia, Mariaconcetta Canico, Alberto Roncaglia, Pablo Cancio Pastor, Paolo De Natale has patent issued to Assignee. If there are other authors, they declare that they have no known competing financial interests or personal relationships that could have appeared to influence the work reported in this paper.

Data availability

Data will be made available on request.

Appendix A. Fabrication process of the mems structures

As summarized in Fig. A.7, the analyzed structures were fabricated in a silicon-on-insulator wafer (SOI) made up of a 10 μm thick Si device layer and a 500 μm thick Si handle layer separated by a 2 μm thick buried SiO_2 **(a)**.

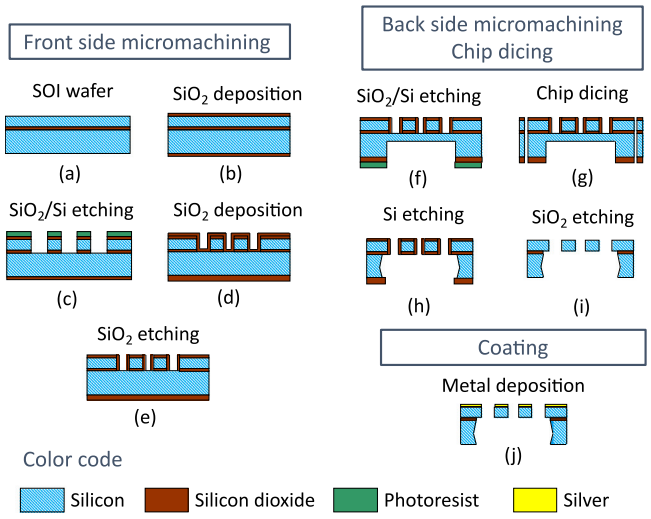

Fig. A.7. Graphical description of the routine used to fabricate the investigated Micro-Electro-Mechanical structures.

The structure's layouts were created on the front side by photolithography and dry etching of the Si device layer through a 4 μm-thick OIR-908 35 photoresist on a 2.2 μm-thick SiO_2 hard mask **(b, c)**. The obtained Si trenches were uniformly coated by a 35 nm thick polysilicon layer, which was afterward overoxidized to form a 180 nm-thick SIO_2 conformal layer all around the patterned MEMS geometry. The surface was further coated with 1.5 μm SiO_2 deposited by LPCVD so that the resulting SiO_2 layer on the top surface was about 3.6 μm **(d)**. Then, a maskless Inductively Coupled Plasma (ICP) etch-back step was performed to complete the removal of the previously deposited 1.7 μm-thick SiO_2 layer from the bottom of the trenches **(e)**. As a result, the trenches originating the MEMS structures were protected by a SiO_2 coating during the subsequent backside wet etching **(h)**, without creating any free-standing SiO_2 membranes between the released Si structures. In this way, possible problems coming from cracking of these membranes after the release of the MEMS resonators were prevented.

After frontside micromachining, pass-through holes were created in the handle layer from the backside of the wafer, to release the MEMS resonators and, at the same time, to guarantee optical access to them for vibration sensing. The backside holes were opened by Si etching through the 3.5 μm thick back side SiO_2 **(f)**. The Si removal was achieved in two steps: first, with a Deep Reactive Ion Etching (DRIE) process up to 325 μm depth **(f)**; then, after wafer cutting **(g)**, using an anisotropic wet etching in tetramethylammonium hydroxide (TMAH) performed on diced chips **(h)**. The two-step etching allowed for secure chip separation by dicing saw. The structures were finally released by SiO_2 wet etching **(i)**. The MEMS reflectance was maximized by a 40 nm thick Ag layer evaporated on the front side **(k)**.

For the Si DRIE foreseen at steps **(c)** and **(f)** in the flow, a Bosch process providing a 5 μm/min etch rate on Si was used. The gas mixture was made up of 300 sccm SF_6 and 150 sccm C_4F_8, at 0.027 mbar chamber pressure.

The Si anisotropic wet etching performed at step **(h)**, was carried out in a 5% wt and diluted aqueous TMAH solution with the addition of 0.5% wt. ammonium peroxidisulfate, following the procedure described in [41]. The solution was uniformly heated at 90 °C and stirred at 1000 rpm. The etching duration, up to the complete release of the structures, exceeded 1h 40 min. For SiO_2 DRIE, 17 sccm C_4F_8 were fluxed in the chamber at 0.005 mbar pressure, resulting in an etch rate of about 0.25 μm/min. This process was used in steps **(c)** and **(e)**. A SiO_2 wet etching was performed at step **(i)** using either a commercial buffered oxide etch (BOE) solution or hydrofluoric acid diluted in water.

LPCVD polysilicon was deposited at 610 °C in 80 sccm SiH_4 flow at 0.21 mbar. The deposition rate ranged between 11.7 nm/min and 13.7 nm/min. The polysilicon was wet oxidized at 1100 °C. These processes were used to fabricate the passivation coating shown at step **(e)**. LPCVD SiO_2 was deposited at steps **(b)** and **(d)** with the following parameters: 430 °C chamber temperature, 0.24 mbar chamber pressure, in a 82 sccm SiH_4 and 120 sccm O_2 gas mixture. The resulting SiO_2 deposition rate was around 1 μm/h.

Appendix B. Q-factors and resonance frequencies with pressure

This appendix allows the reader to have an overall look at the dependence of both the resonance frequency and the quality factor with the working pressure. As previously stated in Section 4.1, the resonance frequency is one of the parameters that can be extracted from the Lorentzian fit on the resonant curve spectrum of a given MEMS at a fixed pressure.

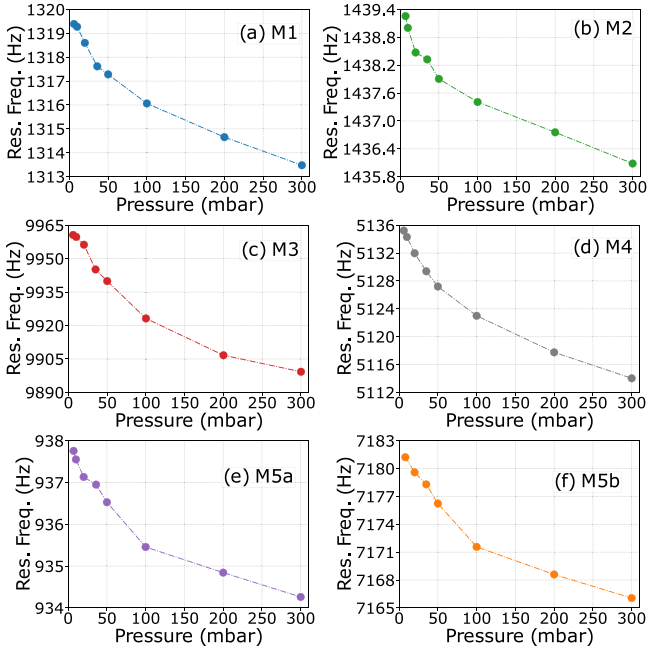

Fig. B.8. Resonance frequency versus working pressure for: **(a)** M1, **(b)** M2, **(c)** M3, **(d)** M4, **(e)** M5a, and **(f)** M5 7b. As it is possible to see, the resonant frequency decreases when increasing the pressure.

Fig. B.8 shows a clear decrease in the resonance frequency with increasing pressure for all the structures investigated. This occurs because the gas in which they are immersed acts as a viscous fluid whose damping effect increases when the pressure increases. Since the presence of the surrounding gas introduces a force that causes energy dissipation on the vibrating body [32], this effect is also responsible for the Q-factor degradation.

Fig. B.9 clearly shows that for all the structures studied the experimental variation of the Q-factor with the pressure (colored data points in the graphs) follows a trend (black dashed line) determined by this damping effect and whose mathematical formula is given by [31]:

$$Q(P) = A + \frac{cQ_0}{a + bQ_0\sqrt{P}}, \tag{B.1}$$

Here Q_0 is the quality factor in vacuum, which includes all the pressure-independent loss mechanisms (such as thermoplastic damping) [33], while A, a, b, and c are fitting parameters that take into account both the geometry of the MEMS and the viscosity of the surrounding fluid.

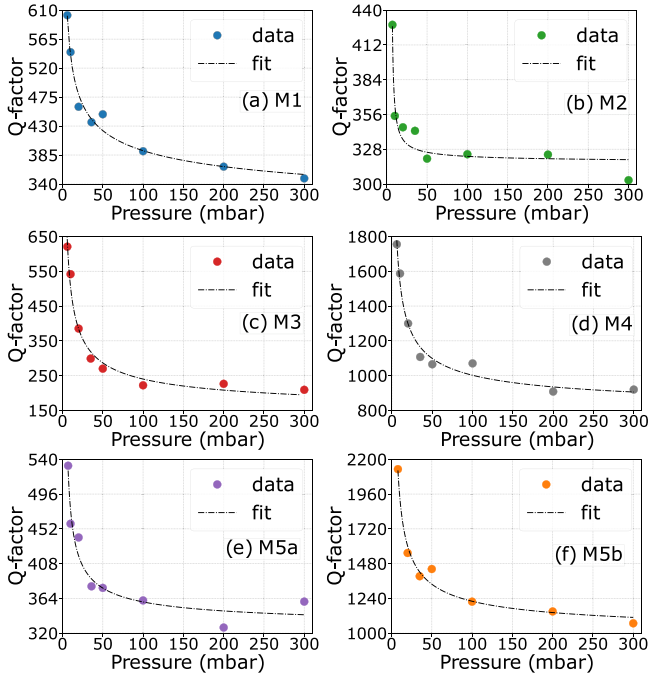

Fig. B.9. Q-factor versus working pressure for: **(a)** M1, **(b)** M2, **(c)** M3, **(d)** M4, **(e)** M5a, and **(f)** M5b. For each graph, the colored dots represent the experimental data obtained as already explained in Section 4.1, while the black dashed line is the fit on the data.

Appendix C. Photo-acoustic signal with pressure

For completeness, in this appendix are reported all the photo-acoustic spectra associated with the six investigated cases. Looking at Fig. C.10 it is possible to notice that in all the cases the photo-acoustic signal increases from low pressure (around 5 mbar) until it reaches its maximum at a pressure within the range of 20 to 50 mbar. Then it starts to rapidly decrease for higher values of working pressure. Furthermore, the spectra depicted in Figs. C.10**(a)**, **(b)**, and **(e)**, respectively associated with the structures M1, M2, and M5a, are characterized by a higher average noise level on the tails compared to the other structures. This corresponds to the higher SNR shown by the M3, M4, and M5b structures working at higher frequencies, as described in the main text.

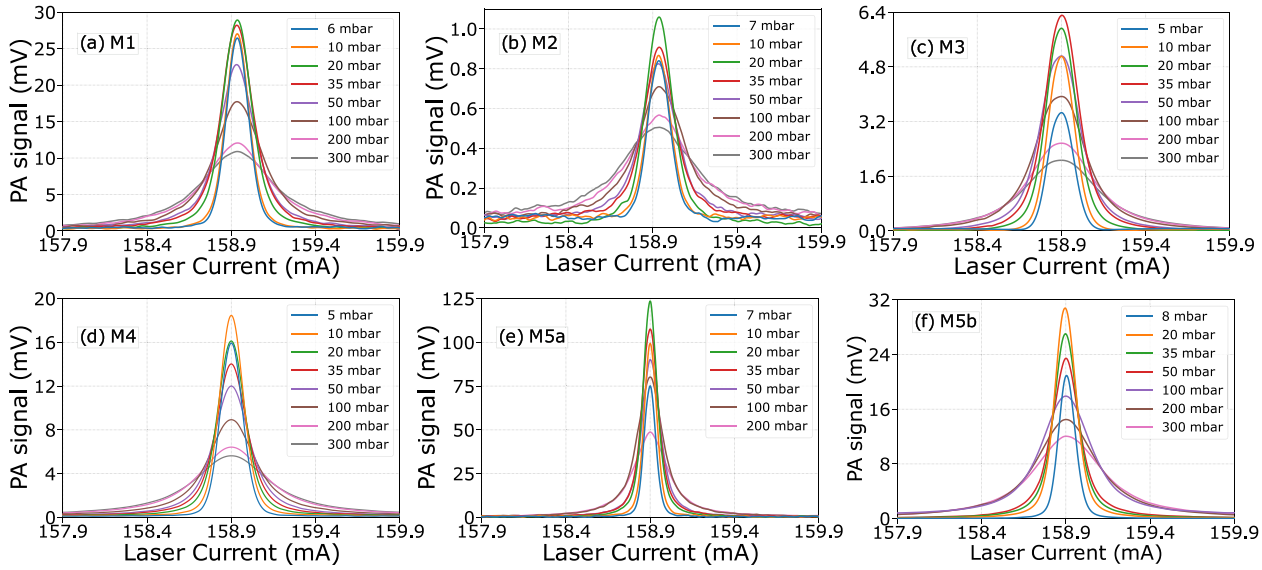

Fig. C.10. 1f photo-acoustic traces at different pressures for: **(a)** M1, **(b)** M2, **(c)** M3, **(d)** M4, **(e)** Ma, and **(f)** M5b.

References

[1] Shaobin Feng, Fadi Farha, Qingjuan Li, Yueliang Wan, Yang Xu, Tao Zhang, Huansheng Ning, Review on smart gas sensing technology, Sensors 19 (17) (2019) 3760.

[2] Nader Zare-Shehneh, Fariba Mollarasouli, Mehrorang Ghaedi, Recent advances in carbon nanostructure-based electrochemical biosensors for environmental monitoring, Crit. Rev. Anal. Chem. 53 (3) (2023) 520–536.

[3] Shirong Huang, Alexander Croy, Luis Antonio Panes-Ruiz, Vyacheslav Khavrus, Viktor Bezugly, Bergoi Ibarlucea, Gianaurelio Cuniberti, Machine learning-enabled smart gas sensing platform for identification of industrial gases, Adv. Intell. Syst. 4 (4) (2022) 2200016.

[4] Lloyd E. Emokpae, Roland N. Emokpae Jr., Ese Bowry, Jaeed Bin Saif, Muntasir Mahmud, Wassila Lalouani, Mohamed Younis, Robert L. Joyner Jr., A wearable multi-modal acoustic system for breathing analysis, J. Acoust. Soc. Am. 151 (2) (2022) 1033–1038.

[5] Vijendra Singh Bhati, Vishakha Takhar, Ramesh Raliya, Mahesh Kumar, Rupak Banerjee, Recent advances in g-C3N4 based gas sensors for the detection of toxic and flammable gases: A review, Nano Express 3 (1) (2022) 014003.

[6] Archana Zala, Harshad Patel, Dendrimer enhanced fingerprint and explosive detection: A critical review, Eng. Sci. 20 (2022) 1–13.

[7] Philippe Repond, Markus W. Sigrist, Photoacoustic spectroscopy on trace gases with continuously tunable CO 2 laser, Appl. Optics 35 (21) (1996) 4065–4085.

[8] Davide Pinto, Harald Moser, Johannes P. Waclawek, Stefano Dello Russo, Pietro Patimisco, Vincenzo Spagnolo, Bernhard Lendl, Parts-per-billion detection of carbon monoxide: A comparison between quartz-enhanced photoacoustic and photothermal spectroscopy, Photoacoustics 22 (2021) 100244.

[9] M.W. Sigrist, Trace gas monitoring by laser-photoacoustic spectroscopy, Infrared Phys. Technol. 36 (1) (1995) 415–425.

[10] Alaa Fathy, Yasser M. Sabry, Ian W. Hunter, Diaa Khalil, Tarik Bourouina, Direct absorption and photoacoustic spectroscopy for gas sensing and analysis: A critical review, Laser Photonics Rev. 16 (8) (2022) 2100556.

[11] András Miklós, Peter Hess, Zoltán Bozóki, Application of acoustic resonators in photoacoustic trace gas analysis and metrology, Rev. Sci. Instrum. 72 (4) (2001) 1937–1955.

[12] Anatoliy A. Kosterev, Yu A. Bakhirkin, Robert F. Curl, Frank K. Tittel, Quartz-enhanced photoacoustic spectroscopy, Opt. Lett. 27 (21) (2002) 1902–1904.

[13] Klaus Wilcken, Jyrki Kauppinen, Optimization of a microphone for photoacoustic spectroscopy, Appl. Spectrosc. 57 (9) (2003) 1087–1092.

[14] Haoyang Lin, Yihua Liu, Leqing Lin, Wenguo Zhu, Xu Zhou, Yongchun Zhong, Marilena Giglio, Angelo Sampaolo, Pietro Patimisco, Frank K. Tittel, et al., Application of standard and custom quartz tuning forks for quartz-enhanced photoacoustic spectroscopy gas sensing, Appl. Spectrosc. Rev. 58 (8) (2023) 562–584.

[15] Shuchao Wang, Marcel Hoffmann, Ali K. Yetisen, Kun Wang, Franziska Brändle, Wolfgang Kurz, Martin Jakobi, Quan Zhou, Alexander W. Koch, Optical interferometer-based methods for photoacoustic gas sensing: A review, Appl. Spectrosc. Rev. (2023) 1–40.

[16] Xueshi Zhang, Lixian Liu, Yanyan Liu, Le Zhang, Xukun Yin, Huiting Huan, Teli Xi, Xiaopeng Shao, Detectors for gas-phase photoacoustic spectroscopy: A review, Microw. Opt. Technol. Lett. 65 (5) (2023) 1535–1544.

[17] Pietro Patimisco, Angelo Sampaolo, Marilena Giglio, Stefano Dello Russo, Verena Mackowiak, Hubert Rossmadl, Alex Cable, Frank K. Tittel, Vincenzo Spagnolo, Tuning forks with optimized geometries for quartz-enhanced photoacoustic spectroscopy, Opt. Express 27 (2) (2019) 1401–1415.

[18] Huadan Zheng, Yihua Liu, Haoyang Lin, Bin Liu, Xiaohang Gu, Dongquan Li, Bincheng Huang, Yichao Wu, Linpeng Dong, Wenguo Zhu, et al., Quartz-enhanced photoacoustic spectroscopy employing pilot line manufactured custom tuning forks, Photoacoustics 17 (2020) 100158.

[19] Maxime Duquesnoy, Guillaume Aoust, Jean-Michel Melkonian, Raphaël Lévy, Myriam Raybaut, Antoine Godard, Quartz enhanced photoacoustic spectroscopy based on a custom quartz tuning fork, Sensors 19 (6) (2019) 1362.

[20] Sheng Zhou, Martin Slaman, Davide Iannuzzi, Demonstration of a highly sensitive photoacoustic spectrometer based on a miniaturized all-optical detecting sensor, Opt. Express 25 (15) (2017) 17541–17548.

[21] Min Guo, Ke Chen, Beilei Yang, Guangyin Zhang, Xinyu Zhao, Chenxi Li, Miniaturized anti-interference cantilever-enhanced fiber-optic photoacoustic methane sensor, Sensors Actuators B 370 (2022) 132446.

[22] Zhengyuan Zhang, Xinhong Fan, Yufu Xu, Yongqi Wang, Yiyao Tang, Rui Zhao, Chenxi Li, Heng Wang, Ke Chen, Silicon-cantilever-enhanced single-fiber photoacoustic acetylene gas sensor, Sensors 23 (17) (2023) 7644.

[23] A.A. Kosterev, Y.A. Bakhirkin, F.K. Tittel, S. McWhorter, B. Ashcraft, QEPAS methane sensor performance for humidified gases, Appl. Phys. B 92 (2008) 103–109.

[24] F.K. Tittel, Influence of molecular relaxation dynamics on quartz-enhanced photoacoustic detection of CO2 at $\lambda = 2$ μm, Appl. Phys. B 85 (2006) 301–306.

[25] Andrea Zifarelli, Marilena Giglio, Giansergio Menduni, Angelo Sampaolo, Pietro Patimisco, Vittorio M.N. Passaro, Hongpeng Wu, Lei Dong, Vincenzo Spagnolo, Partial least-squares regression as a tool to retrieve gas concentrations in mixtures detected using quartz-enhanced photoacoustic spectroscopy, Anal. Chem. 92 (16) (2020) 11035–11043.

[26] Andrea Zifarelli, Aldo Francesco Pio Cantatore, Angelo Sampaolo, Max Mueller, Thomas Rueck, Christine Hoelzl, Hubert Rossmadl, Pietro Patimisco, Vincenzo Spagnolo, Multivariate analysis and digital twin modelling: Alternative approaches to evaluate molecular relaxation in photoacoustic spectroscopy, Photoacoustics 33 (2023) 100564.

[27] Wan-Thai Hsu, Recent progress in silicon MEMS oscillators, in: Proceedings of the 40th Annual Precise Time and Time Interval Systems and Applications Meeting, 2008, pp. 135–146.

[28] V. Koskinen, J. Fonsen, K. Roth, J. Kauppinen, Progress in cantilever enhanced photoacoustic spectroscopy, Vib. Spectrosc. 48 (1) (2008) 16–21.

[29] Lujun Fu, Ping Lu, Chaotan Sima, Jinbiao Zhao, Yufeng Pan, Tailin Li, Xiaohang Zhang, Deming Liu, Small-volume highly-sensitive all-optical gas sensor using non-resonant photoacoustic spectroscopy with dual silicon cantilever optical microphones, Photoacoustics 27 (2022) 100382.

[30] Mario Siciliani de Cumis, Simone Borri, Mariaconcetta Canino, Pablo Cancio Pastor, Paolo De Natale, Inaki Lopez Garcia, Alberto Roncaglia, Photoacoustic spectroscopy sensor for trace gas detection and method for trace gas detection, patent pending WO2023126455A1.

[31] P. Patimisco, A. Sampaolo, L. Dong, M. Giglio, Gaetano Scamarcio, F.K. Tittel, V. Spagnolo, Analysis of the electro-elastic properties of custom quartz tuning forks for optoacoustic gas sensing, Sensors Actuators B 227 (2016) 539–546.

[32] Pietro Patimisco, Angelo Sampaolo, Verena Mackowiak, Hubert Rossmadl, Alex Cable, Frank K. Tittel, Vincenzo Spagnolo, Loss mechanisms determining the quality factors in quartz tuning forks vibrating at the fundamental and first overtone modes, IEEE Trans. Ultrason. Ferroelectr. Freq. Control 65 (10) (2018) 1951–1957.

[33] Stefano Dello Russo, Angelo Sampaolo, Pietro Patimisco, Giansergio Menduni, Marilena Giglio, Christine Hoelzl, Vittorio M.N. Passaro, Hongpeng Wu, Lei Dong, Vincenzo Spagnolo, Quartz-enhanced photoacoustic spectroscopy exploiting low-frequency tuning forks as a tool to measure the vibrational relaxation rate in gas species, Photoacoustics 21 (2021) 100227.

[34] Adv Van der Ziel, Flicker noise in electronic devices, in: Advances in Electronics and Electron Physics, vol. 49, Elsevier, 1979, pp. 225–297.

[35] Raffaele De Palo, Arianna Elefante, Gabriele Biagi, Francesco Paciolla, Robert Weih, Valeria Villada, Andrea Zifarelli, Marilena Giglio, Angelo Sampaolo, Vincenzo Spagnolo, et al., Quartz-enhanced photoacoustic sensors for detection of eight air pollutants, Adv. Photon. Res. (2023) 2200353.

[36] Michal Dostál, Jan Suchánek, Václav Válek, Zuzana Blatoňová, Václav Nevrlý, Petr Bitala, Pavel Kubát, Zdeněk Zelinger, Cantilever-enhanced photoacoustic detection and infrared spectroscopy of trace species produced by biomass burning, Energy & Fuels 32 (10) (2018) 10163–10168.

[37] Huixiao Pan, Zheyan Zhou, Shiyu Zhang, Fan Wang, Jing Wei, N2O emissions from aquatic ecosystems: A review, Atmosphere 14 (8) (2023) 1291.

[38] Stefano Dello Russo, Marilena Giglio, Angelo Sampaolo, Pietro Patimisco, Giansergio Menduni, Hongpeng Wu, Lei Dong, Vittorio M.N. Passaro, Vincenzo Spagnolo, Acoustic coupling between resonator tubes in quartz-enhanced photoacoustic spectrophones employing a large prong spacing tuning fork, Sensors 19 (19) (2019) 4109.

[39] S. Borri, P. Patimisco, I. Galli, D. Mazzotti, G. Giusfredi, N. Akikusa, M. Yamanishi, Gaetano Scamarcio, P. De Natale, V. Spagnolo, Intracavity quartz-enhanced photoacoustic sensor, Appl. Phys. Lett. 104 (9) (2014).

[40] Zhen Wang, Qiang Wang, Hui Zhang, Simone Borri, Iacopo Galli, Angelo Sampaolo, Pietro Patimisco, Vincenzo Luigi Spagnolo, Paolo De Natale, Wei Ren, Doubly resonant sub-ppt photoacoustic gas detection with eight decades dynamic range, Photoacoustics 27 (2022) 100387.

[41] S. Brida, A. Faes, V. Guarnieri, F. Giacomozzi, B. Margesin, M. Paranjape, G.U. Pignatel, M. Zen, Microstructures etched in doped TMAH solutions, Microelectron. Eng. 53 (1) (2000) 547–551.

Jacopo Pelini obtained his Master's Degree in Physics in 2021 from the University of Perugia. Currently, he is a Ph.D. student in Quantum Technologies at the University "Federico II" of Naples, and CNR-INO in Florence. His research focuses on Cantilever-Enhanced photo-acoustic spectroscopy, Micro-Electro-Mechanical Systems characterization, and frequency stabilization of semiconductor mid-infrared laser sources.

Stefano Dello Russo obtained his M.S. degree (cum laude) in Physics in 2018 from the University of Bari. From the same year, he is a Ph.D. student at the Physics Department of the University of Bari, developing his research work at PolySense Lab, joint-research laboratory between Technical University of Bari and THORLABS GmbH. Currently, he is working as a researcher at the Italian Space Agency (ASI). His research activity is focused on Spectroscopy, Metrology and Quantum Communications.

Inaki Lopez Garcia received his Ph.D. in Physic from Complutense University of Madrid (Spain) in 2014. He has worked, and collaborated for several institutes at Italian research council (CNR). His research interests include nanophysics, gas sensing, nonlinear optics, electron microscopy and phase change memories. His work has been published in several peer-reviewed journals.

Maria Concetta Canino, Ph.D. in Physics since 2007, joined the Institute for Microelectronics and Microsystems of CNR in 2008. Since 2018 she is permanent staff. In her research, she studies the physics of the fabrication processes of silicon-based and silicon carbide-based microelectronic devices and advanced solar cells with special focus on material doping.

Alberto Roncaglia received a M. Sc. Degree (cum laude) in Electrical Engineering and a Ph. D. degree in Electronics and Computer Science in 1998 and 2002, respectively, both from the University of Bologna. In 2001 he joined the Institute of Microelectronics and Microsystems (IMM) of the Italian National Research Council (CNR) as a scientific researcher. He has been involved in several EUfunded projects, such as Underground M3 (Eurocores ESF Programme), ROBOSPECT (FP7-ICTRobotics), SiNERGY (FP7-NMP), AEROBI (H2020-ICT-Robotics), Q-SORT (H2020-FETOPEN), RESIST (H2020-MG), SiC Nano for PicoGeo (H2020-FETOPEN), 5D NanoPrinting (H2020FETOPEN), MOLIERE (EIT Manufacturing 2022). His research interests include design, simulation and technology development for the fabrication of micro- and nano-electro-mechanical systems (MEMS and NEMS).

Pablo Cancio Pastor received the Graduate degree in physics from Complutense University of Madrid in 1986, and the Ph.D. degree in physics from the Autonoma University of Madrid in 1992. At present, he is a permanent Staff Researcher of the National Institute of Optics, Italian National Research Council, Florence (CNR-INO). He is an expert in state-of-the-art laser sources in the visible-infrared spectral regions including optical frequency combs, nonlinear optical generated coherent sources, semiconductor diode lasers and quantum-cascade lasers. His current research interests include high-precision and high-sensitivity atomic and molecular spectroscopy by using high-resolution laser spectrometers.

Iacopo Galli was born in Firenze (Italy), in 1976. He received the Laurea degree in physics. In 2004 and the Ph.D. degree in physics in 2009 from the University of Florence. Since 2004 he works for INO-CNR:
2012 - Research scientist at the Italian National Research Council - Institute of Optics (CNR-INO).
2023 - Senior research scientist at the Italian National Research Council - Institute of Optics (CNRINO).
2016 - Cofounder of ppqSense S.r.l.
His main research interests include nonlinear optics, high-sensitivity and high-precision infrared spectroscopy, frequency metrology, and quantum cascade lasers.

Wei Ren received the B.S. degree in Mechanical Engineering and Automation from Tsinghua University, Beijing, China, in 2006, and the Ph.D. degree in Mechanical Engineering from Stanford University, Stanford, CA, USA, in 2013. He is currently an Associate Professor with the Department of Mechanical and Automation Engineering, The Chinese University of Hong Kong, Hong Kong. His research interests include laser spectroscopy, optical sensing, and combustion and propulsion. He is a Senior Member of Optica.

Paolo De Natale is research director at the National Institute of Optics-INO (Italian CNR) and member of the Directive Council of LENS, Firenze, Italy. In the years 2007–2021 was director of the National Institute of Optics of the Italian National Research Council (INO-CNR, former INOA). He is the Italian representative in the Quantum Community Network (QCN) Board of the EU Flagship on Quantum Technologies and in the Optronics CapTech of the European Defense Agency-EDA. Scientific interests include photonics, atomic and molecular physics, nonlinear optics and quantum technologies. He is author of more than 360 publications, owns 9 patents and is a cofounder of two former CNR spin-off companies, ppqSense srl and QTI srl. He is Fellow of IEEE (since 2011) and OSA (since 2015).

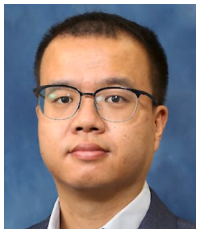

Zhen Wang is currently a research assistant professor at the Chinese University of Hong Kong. He received his Ph.D. degree from the Chinese University of Hong Kong. After that, he worked as a postdoc at the National Institute of Optics (CNR-INO) in Italy. His research interests are trace gas sensing and laser spectroscopy.

Simone Borri completed his Ph.D. in 2007 from the University of Firenze, Italy. He has been a researcher at CNR-National Institute of Optics since 2010. He worked as a researcher for LENS, the European Laboratory for Nonlinear Spectroscopy, and IFN, the Italian Institute for Photonics and Nanotechnologies. His main expertise is in the development of coherent sources and techniques for high-sensitivity and high-resolution molecular spectroscopy in the mid-infrared. After demonstrating the first cavity-enhanced QEPAS system, he is now working on high-performing CEPAS sensors combining mid-infrared lasers, custom-made cantilevers, and high-finesse resonant cavities.

Mario Sicilani de Cumis, Ph.D. in Physics at University of Catania and LENS. He was postdoctoral researcher at CNR in Florence from 2009 to 2015 and temporary researcher at INRIM in Turin until 2016. From 2017 he is permanent researcher at ASI in Matera. His activities concern experiments about Nonlinear Optics, Spectroscopy, Sensors, Metrology, Laser and Quantum Technologies. He is author of a patent on Photoacoustics sensors and about 50 papers on peer-reviewed journals collecting over 1000 citations.